EDGE ARTICLE

Check for updates

A solid composite electrolyte based on three-dimensional structured zeolite networks for high-performance solid-state lithium metal batteries

Zhaodi Luo,[a] Yuxin Cui,[ab] Zixuan Zhang,[a] Malin Li [ID] *[a] and Jihong Yu [ID] *[ab]

Solid polymer electrolytes (SPEs) are regarded as promising candidates for next-generation solid-state lithium metal batteries (SSLMBs) due to their high flexibility and excellent processability, whereas their practical application remains a challenge to simultaneously achieve high ionic conductivity, superior inherent stability, and desirable interfacial compatibility with the Li metal anode. Here, we report a composite solid electrolyte (CSE) incorporating a three-dimensional zeolite network (3D Zeo) into a poly(ethylene oxide) (PEO) matrix containing lithium bis(trifluoromethanesulfonyl)imide (LiTFSI) salt (3D Zeo/PEO). The interconnected 3D Zeo provides continuous Li^+-conduction pathways and promotes the amorphization of the polymer and the dissociation of the Li salt *via* Lewis acid–base interactions. The resulting 3D Zeo/PEO CSE exhibits an ionic conductivity of 1.62×10^{-4} S cm^{-1} at room temperature and an electrochemical stability window up to 5.7 V *vs.* Li^+/Li, significantly surpassing those of LiTFSI–PEO SPE (3.23×10^{-6} S cm^{-1}, 4.9 V). Leveraging the regulatory effect of the 3D Zeo/PEO CSE on Li^+ deposition and solid electrolyte interphase formation, the symmetric cell demonstrates stable cycling over 2300 h with an overpotential of 0.13 V, and the full cells also deliver superior high-rate capability and long-term stability with a capacity retention of 92% after 500 cycles at room temperature, far exceeding the performance of batteries using LiTFSI–PEO SPE and CSE with zeolite-based particle fillers. This work provides a promising approach for the design of CSEs to achieve high interfacial compatibility and uniform Li^+ deposition for next-generation SSLMBs.

Introduction

With the accelerating global transition toward carbon neutrality, the development of next-generation energy storage systems with superior safety, high energy density, and long-term reliability has become a critical priority to achieve efficient storage and utilization of renewable energy.[1] Among various battery technologies, lithium metal batteries (LMBs) are considered some of the most promising candidates for high-performance applications, owing to the ultrahigh theoretical capacity (3860 mAh g^{-1}), lowest electrochemical potential (−3.04 V *vs.* standard hydrogen electrode), and ultralight density (0.534 g cm^{-3}) of the lithium metal anode.[2–4] Despite their compelling theoretical advantages, LMBs still confront severe challenges including inevitable growth of lithium dendrites, continuous evolution of solid electrolyte interphases (SEIs), and severe parasitic side reactions between conventional liquid electrolytes and the lithium metal anode.[5–8] These issues result in low coulombic efficiency, rapid capacity degradation, and critical thermal runaway risks of LMBs. Furthermore, the intrinsic flammability and electrochemical instability of liquid electrolytes further exacerbate these concerns, particularly under high-voltage or fast-charging conditions.[9,10]

Replacing flammable liquid electrolytes with solid-state electrolytes (SSEs) represents an effective approach to achieve the safety and stability of LMBs.[11] In comparison with other practical industrialization routes for SSEs, poly(ethylene oxide) (PEO)-based solid polymer electrolytes (SPEs) have garnered significant attention due to their flexible ethylene oxide chains that offer abundant Li^+ coordination sites, along with their light-weight feature, low interfacial resistance, and excellent processability.[12] However, their practical deployment remains hindered by several inherent limitations. The semi-crystalline nature of PEO restricts segmental motion, resulting in poor ionic conductivity (10^{-8}–10^{-6} S cm^{-1}) at room temperature (RT).[13,14] Additionally, the narrow electrochemical stability window of PEO-based SPEs (<3.8 V) leads to oxidative degradation at high voltages, impeding their compatibility with high-voltage cathodes.[13] In addition, PEO fails to form a robust SEI layer at the interface with the lithium metal anode, which compromises interfacial stability and facilitates dendrite formation.

[a]State Key Laboratory of Inorganic Synthesis and Preparative Chemistry, College of Chemistry, Jilin University, Changchun 130012, P. R. China. E-mail: jihong@jlu.edu.cn; malinli@jlu.edu.cn

[b]International Center of Future Science, Jilin University, Changchun 130012, P. R. China
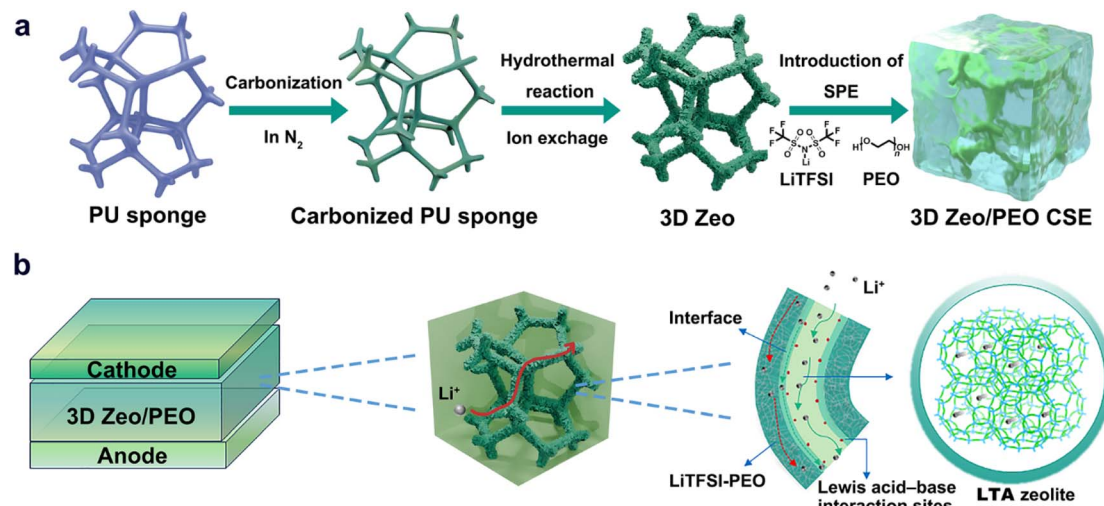
Fig. 1 Schematic illustration of (a) the preparation process for 3D Zeo/PEO CSE and (b) the Li$^+$ conduction pathways in 3D Zeo/PEO CSE.

To overcome the inherent limitations of PEO-based SPEs, the fabrication of composite solid electrolytes (CSEs) by incorporating inorganic SSEs with high ionic conductivity into the PEO matrix has emerged as a compelling strategy. For instance, Zhao *et al.* introduced Al-doped Li$_{6.75}$La$_3$Zr$_{1.75}$Ta$_{0.25}$O$_{12}$ into a lithium bis(trifluoromethanesulfonyl)imide (LiTFSI)–PEO matrix, which significantly enhanced the ionic conductivity (1.12×10^{-5} S cm^{-1} at 25 °C) and electrochemical stability window (5.5 V) due to strong interactions between the inorganic material and the polymer.[15] Wang *et al.* fabricated an interconnected porous Li$_{1.3}$Al$_{0.3}$Ti$_{1.7}$(PO$_4$)$_3$ (LATP) scaffold *via* NaCl templates, which provided continuous Li$^+$ transport channels and simultaneously confined PEO chains to reduce crystallinity.[16] These structural merits led to a high ionic conductivity of 7.47×10^{-4} S cm^{-1} and stable Li plating/stripping cycles over 2000 h at 60 °C. Although significant advancements have been achieved by integrating various ionic conductors into CSEs,[17–21] critical challenges persist in their practical implementation. The majority of conventional inorganic SSEs, such as perovskite Li$_{3x}$La$_{2/3-x}$TiO$_3$, NASICON-type LATP, and sulfide solid electrolytes, suffer from insufficient chemical and electrochemical stability,[22] as well as poor dispersion in PEO, leading to filler aggregation, interfacial resistance, and low ionic conductivity.[23–25] Moreover, the preparation process of these SSEs hardly meets the requirement for constructing continuous ionic conduction pathways, hindering the ion transport between the rigid inorganic particles. Therefore, the rational design of CSEs incorporating inorganic components that combine superior stability, structural interconnectivity, and intrinsic ionic conductivity is vital for realizing high-performance CSEs.

Zeolites, a class of crystalline aluminosilicate materials with well-defined microporous architectures, represent a promising category of inorganic SSEs due to their excellent thermal and electrochemical stability, ionic conduction capability, and electronic insulation property.[26] Notably, the tunable framework composition and surface chemistry of zeolites are beneficial for regulating the dissociation of lithium salts and the crystallinity of polymers, achieving favourable ionic conduction and satisfactory interfacial compatibility between inorganic and polymer components.[27] Unfortunately, most reported systems employ zeolites as randomly dispersed filler particles to construct CSEs, failing to establish continuous pathways for fast Li$^+$ transport through the inorganic phase and thereby undermining the full potential of zeolite-based SSEs.[28–32]

Herein, we fabricate a CSE that couples a three-dimensional structured zeolite network (3D Zeo) within a LiTFSI–PEO matrix, denoted as 3D Zeo/PEO CSE (Fig. 1a). Leveraging the continuous Li$^+$ conduction pathway provided by 3D Zeo (Fig. 1b) and the enhanced polymer–zeolite interfacial interactions, 3D Zeo/PEO CSE exhibits an ionic conductivity of 1.62×10^{-4} S cm^{-1} and an extended electrochemical stability window of 5.7 V *vs.* Li$^+$/Li, significantly surpassing those of the LiTFSI–PEO SPE (3.23×10^{-6} S cm^{-1}, 4.9 V). In addition, the robust porous zeolite networks play a key role in constructing a stable SEI and regulating lithium deposition to suppress dendrite formation, highlighting the superiority of the 3D architecture of the zeolite network compared to the zeolite-based particles that confront challenges to achieve uniform distribution and continuous structure. Consequently, a symmetric Li cell with 3D Zeo/PEO CSE displays a stable lithium stripping/plating cyclic performance for over 2300 h at RT, far exceeding the life spans of cells using the SPE (155 h) and the CSE with zeolite-based powder fillers (580 h). Also, the LiFePO$_4$ (LFP)|3D Zeo/PEO|Li full cell exhibits a capacity retention of 82% after 700 cycles at 60 °C. This work provides a promising strategy for the development of high-performance CSEs by comprehensively considering material selection and structural design, and promotes the practical application of solid-state LMBs with high safety and energy density.

Results and discussion

The fabrication procedure of 3D Zeo/PEO CSE is shown in Fig. 1a. The carbonized polyurethane (PU) sponge was utilized as the template to construct 3D Zeo *via* a hydrothermal reaction and Li-ion exchange process. As shown in Fig. 2a, 3D Zeo exhibits a 3D architecture formed by highly interconnected microwires with a diameter of about 10 μm, retaining the
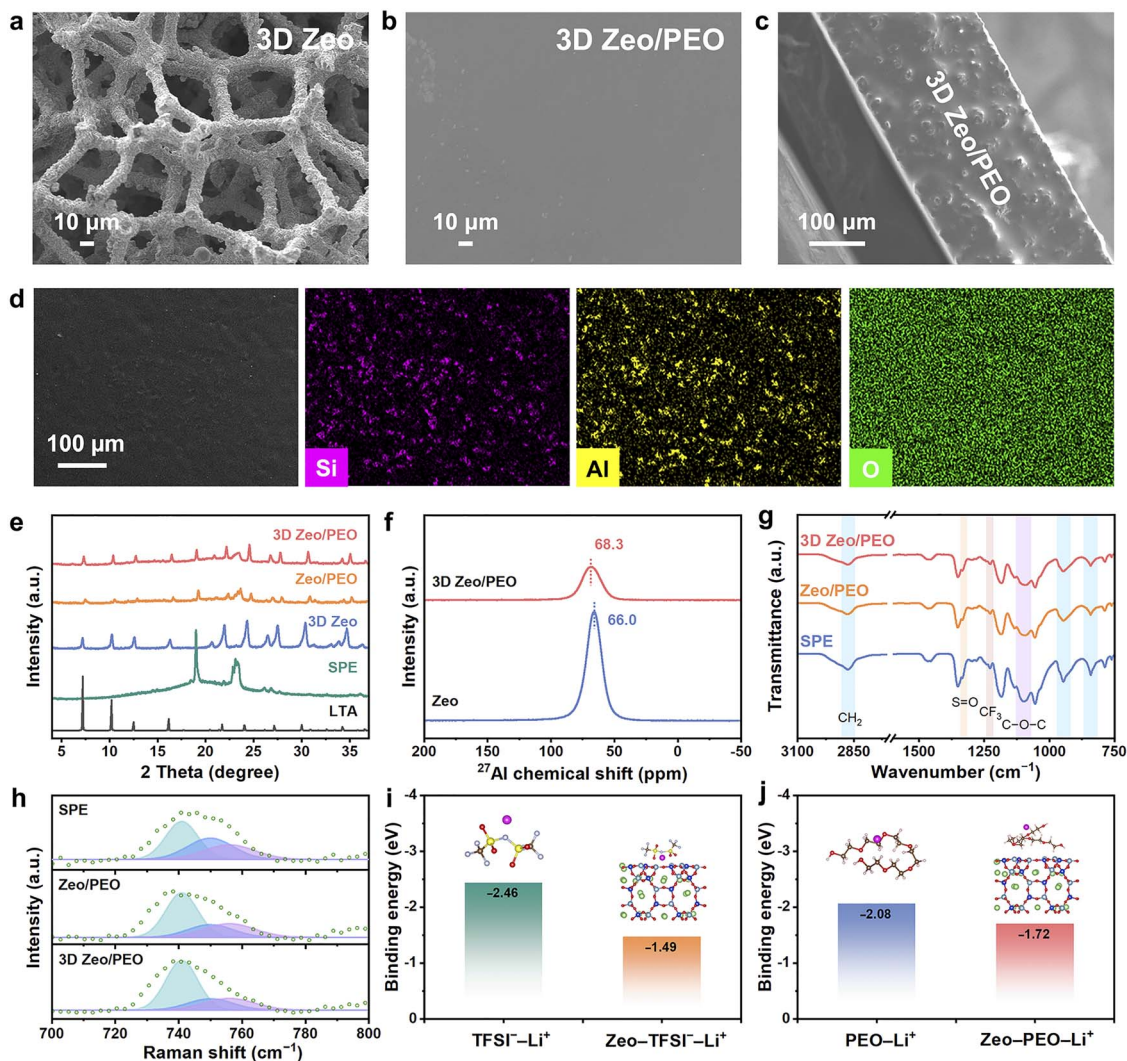
Fig. 2 Top-sectional SEM images of (a) 3D Zeo and (b) 3D Zeo/PEO. (c) Cross-sectional SEM image of 3D Zeo/PEO. (d) EDS element mappings of 3D Zeo/PEO. (e) XRD patterns of SPE, 3D Zeo, Zeo/PEO, and 3D Zeo/PEO; the simulated XRD pattern of **LTA** zeolite is shown for comparison. (f) ^{27}Al solid-state NMR spectra of 3D Zeolite/PEO and Zeo. (g) FTIR spectra and (h) Raman spectra of SPE, Zeo/PEO, and 3D Zeo/PEO. Calculation of binding energies of (i) TFSI$^-$–Li$^+$ and Zeo–TFSI$^-$–Li$^+$, and (j) PEO–Li$^+$ and Zeo–PEO–Li$^+$.

porous morphology of pristine and carbonized PU sponge (Fig. S1 and S2). This open network not only presents exceptional mechanical strength, but also features high surface area and interconnected channels for facile polymer infiltration and extensive interfacial contact between zeolite and polymer components. Moreover, the continuous networks consisting of zeolite can provide efficient conduction pathways for Li$^+$. After being infiltrated by the mixture of PEO and LiTFSI, 3D Zeo is well filled by the polymer matrix to form 3D Zeo/PEO CSE with superior flexibility and a smooth surface (Fig. 2b and S3). The cross-sectional scanning electron microscopy (SEM) image (Fig. 2c) also confirms the excellent interfacial integration between 3D Zeo and the PEO component. Moreover, the energy dispersive spectroscopy (EDS) mappings of 3D Zeo/PEO CSE (Fig. 2d) validate the uniform distribution of the zeolite and polymer interpenetrating network, which is favourable for enabling continuous ionic conduction and robust mechanical strength. For comparison, the LiTFSI–PEO solid polymer

electrolyte (denoted as SPE) and the CSE composed of LiTFSI–PEO and zeolite-based powder (Zeo/PEO) were also prepared. Although Zeo/PEO CSE exhibits a smooth surface similar to that of SPE (Fig. S4), the inherent inhomogeneity of the zeolite-based powder derived from 3D Zeo (denoted as Zeo, Fig. S5) leads to their uneven dispersion in Zeo/PEO (Fig. S6).

X-ray diffraction (XRD) measurements were conducted to reveal the crystallinity and phase evolution of SSEs (Fig. 2e). The XRD pattern of 3D Zeo is consistent with the simulated XRD pattern of A zeolite with **LTA** topology (Fig. S7), indicating the successful crystallization of the zeolite. The XRD pattern of SPE displays two distinct diffraction peaks located at 19.2° and 23.3°, which are ascribed to the crystalline peaks of PEO. As for the Zeo/PEO, the intensity of PEO-associated diffraction peaks decreases, suggesting the reduction of PEO crystallinity due to the Lewis acid–base interaction with the zeolite. Notably, a further decrease in the intensity of PEO-associated diffraction peaks can be observed in the XRD pattern of 3D Zeo/PEO CSE.

This is primarily attributed to the distinct architecture advantages of 3D zeolite networks that can effectively prevent the aggregation of zeolite particles, thereby maintaining extensive active sites for Lewis acid–base interactions between PEO and zeolite to further suppress the crystallization of PEO. Differential scanning calorimetry analysis further confirms the decreased crystallinity of PEO, as the sharp melting peak of crystalline PEO at ~53 °C for SPE shifts to a broader peak at 49 °C for 3D Zeo/PEO (Fig. S8). The ^{27}Al solid-state nuclear magnetic resonance (NMR) spectrum of 3D Zeo/PEO shows a broad peak with a distinct low-field shift in comparison with that of Zeo, directly confirming the proposed Lewis acid–base interactions between the zeolite and LiTFSI–PEO matrix (Fig. 2f). To further elucidate the interfacial interactions within the CSEs, Fourier transform infrared (FTIR) spectra of SPE, Zeo/PEO, and 3D Zeo/PEO were analyzed (Fig. 2g). In the FTIR spectrum of SPE, the bands around 841, 946, and 2876 cm^{-1} correspond to the CH$_2$ wagging, twisting and stretching modes, respectively.[33] The distinct characteristic peaks at 1054, 1098, and 1133 cm^{-1} can be attributed to C–O–C stretching bands, which reflect the crystalline microstructure of PEO.[34–36] These peaks broaden significantly upon zeolite incorporation, particularly in the 3D Zeo/PEO system, indicating reduced polymer crystallinity and enhanced amorphous segmental mobility of PEO. A notable redshift of the 1098 cm^{-1} band is observed in the FTIR spectrum of 3D Zeo/PEO, suggesting Lewis acid–base interactions between the zeolite surface and ether oxygen atoms. Such spectral changes are less pronounced in the spectrum of Zeo/PEO, probably arising from the poor dispersion of zeolite particles and limited interface contact.

In addition, the peak associated with S=O stretching vibration from LiTFSI (1334 cm^{-1}) tends to be broad after incorporating 3D Zeo into PEO, and the CF$_3$ stretching band (1228 cm^{-1}) shifts slightly to a lower wavenumber, which indicates enhanced LiTFSI dissociation.[36] Raman spectroscopy was performed to further investigate the coordinating configuration of TFSI$^-$ (Fig. 2h). The Raman shift region around 720–780 cm^{-1} reveals distinct coordination states of the TFSI$^-$ anion, with bands at 741, 750, and 756 cm^{-1} corresponding to free TFSI$^-$, contact ion pairs, and aggregates, respectively.[37,38] Compared to the spectrum of SPE, Raman spectra of both Zeo/PEO and 3D Zeo/PEO CSEs exhibit a higher intensity ratio of free TFSI$^-$, indicating an increased degree of salt dissociation. This enhancement is attributed to the interaction between the zeolite and LiTFSI–PEO matrix, which promotes Li$^+$ solvation to achieve high ionic conductivity. Notably, 3D Zeo/PEO shows the highest proportion of free TFSI$^-$ among all samples, underscoring the structural advantage of the 3D network. ^{7}Li NMR results also confirm the enhanced dissociation of LiTFSI. As shown in Fig. S9, the ^{7}Li chemical shift of the 3D Zeo/PEO CSE ($\delta = 0.7$ ppm) is notably downfield shifted compared to that of SPE ($\delta = 0.1$ ppm), revealing reduced electron cloud density around Li$^+$ and loosened coordination with electron-donating nitrogen in TFSI$^-$ anions.

To gain further understanding on the coordination states within 3D Zeo/PEO CSE, density functional theory (DFT) calculations were conducted to comprehensively explore the microscopic interactions among PEO, LiTFSI, and zeolite-based components. As shown in Fig. S10, zeolite exhibits a less negative adsorption energy (E_{ad}) for Li$^+$ (−1.80 eV) and a more negative E_{ad} for TFSI$^-$ (−2.57 eV) compared to those of PEO (−2.08 eV for Li$^+$ and −1.73 eV for TFSI$^-$). The results indicate a weaker interaction between Li$^+$ and the zeolite framework, which may facilitate facile migration of Li$^+$. In contrast, the stronger interaction between zeolites and TFSI$^-$ is favorable to promote the dissociation of LiTFSI and confine the migration of TFSI$^-$, which can significantly enhance the concentration of free Li$^+$ and effectively promote efficient Li$^+$ conduction to achieve superior Li$^+$ transference numbers (t_{Li^+}). Additionally, the binding energy of Li$^+$ with TFSI$^-$ becomes more positive after the addition of the zeolite (Fig. 2i), suggesting a higher dissociation degree of LiTFSI and thus enhancing the Li$^+$ mobility. This calculation result is consistent with the experimental results of FTIR and Raman spectra. In virtue of the interaction between the zeolite and PEO, the binding force between Li$^+$ and ether oxygens in PEO is considerably weakened with the presence of the zeolite, which demonstrates a higher Li$^+$ mobility in 3D Zeo/PEO CSE (Fig. 2j). Thus, these comprehensive experimental and computational results indicate that 3D Zeo can effectively modulate both polymer segmental dynamics and ionic coordination environments, ultimately contributing to enhanced Li$^+$ conduction capabilities.

The thermal stability of CSEs plays a key role in ensuring the stable and safe operation of solid-state LMBs. As shown in Fig. S11, pristine SPE membranes undergo visible softening and shrinkage after exposure to elevated temperatures, while the deformation is markedly suppressed in zeolite-containing systems, particularly with 3D Zeo. 3D Zeo/PEO CSE also exhibits enhanced resistance to open flame heating (Fig. S12). Furthermore, thermogravimetric analysis curves (Fig. S13) show a significant increase in the decomposition temperature for 3D Zeo/PEO CSE, indicating the enhanced thermal stability of 3D Zeo/PEO compared with SPE. Overall, the characterization results demonstrate the multifunctional role of 3D Zeo in simultaneously promoting the chain disorder of the polymer phase, facilitating the dissociation of Li salt and increasing the thermal stability of the CSE.

The ionic conductivities of SSEs were estimated via electrochemical impedance spectroscopy (EIS) at different temperatures (Fig. 3a–c). According to the fitting results shown in Fig. 3d and Table S1, the ionic conductivity of each SSE increases with temperature. SPE exhibits an ionic conductivity of ~3.23 × 10^{-6} S cm^{-1} at RT. The zeolite-based CSEs demonstrate a substantial enhancement in ionic conductivity. In particular, the ionic conductivity of 3D Zeo/PEO CSE reaches 1.62 × 10^{-4} S cm^{-1}, which shows a two-order-of-magnitude improvement in comparison with that of SPE. This value further increases to 6.49 × 10^{-4} S cm^{-1} at 60 °C, also exceeding the values of SPE and Zeo/PEO measured at the same temperature. The higher ionic conductivity of 3D Zeo/PEO compared to other SSEs is attributed to the continuous ionic conduction pathways provided by the 3D Zeo, and also originates from the interaction between 3D Zeo and the polymer phase, which increases both the amorphous ratio of PEO and the dissociation of LiTFSI. Moreover, 3D Zeo/PEO
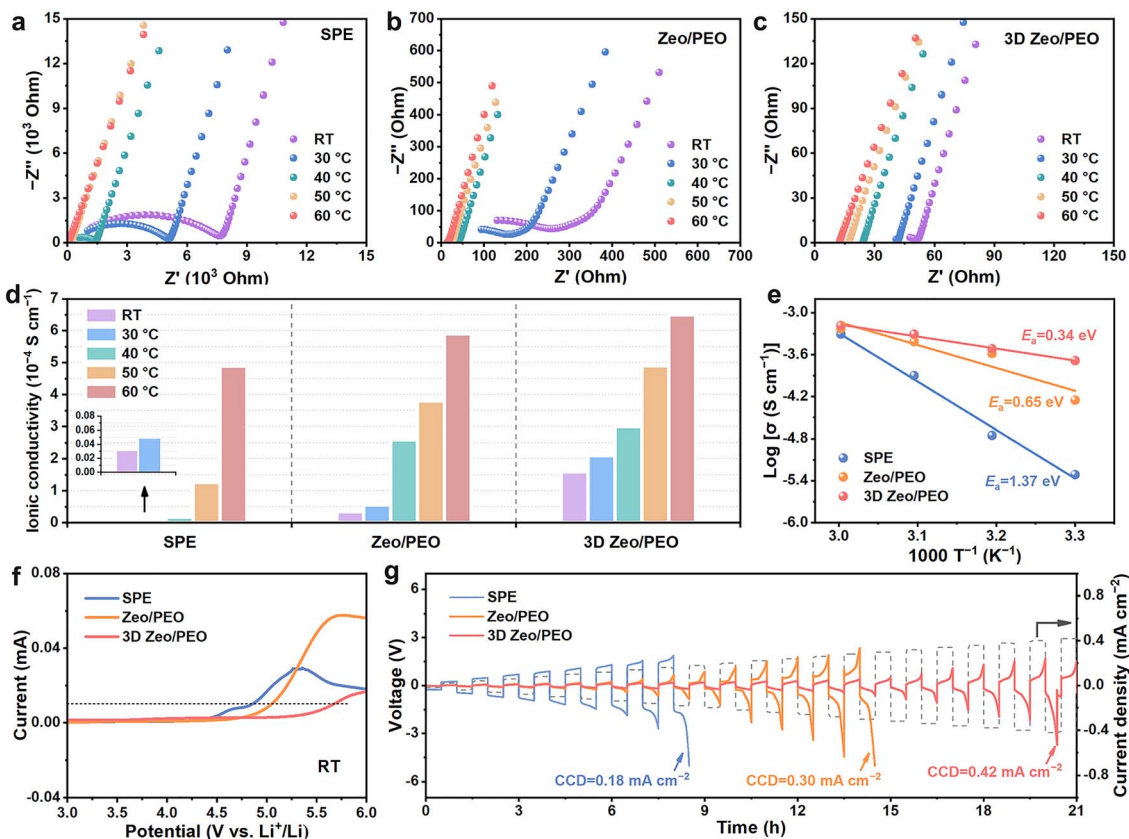
Fig. 3 Nyquist plots of (a) SPE, (b) Zeo/PEO and (c) 3D Zeo/PEO at different temperatures. (d) Comparison of ionic conductivities and (e) the Arrhenius plots of the ionic conductivities for SPE, Zeo/PEO, and 3D Zeo/PEO. (f) LSV and (g) CCD measurements for SPE, Zeo/PEO and 3D Zeo/PEO at RT.

displays the lowest activation energy (E_a) for Li$^+$ transport (0.34 eV), in sharp contrast with those of SPE (1.37 eV) and Zeo/PEO (0.65 eV), which further highlights the coordination capability and the architecture advantages of 3D Zeo (Fig. 3e). Furthermore, 3D Zeo/PEO exhibits a higher t_{Li^+} of 0.42 compared to SPE (0.09) and Zeo/PEO (0.35) as shown in Fig. S14. This result confirms that 3D Zeo can promote effective Li$^+$ migration by confining the transport of TFSI$^-$, in accordance with the previous DFT calculation results. The higher t_{Li^+} of 3D Zeo/PEO facilitates a low overpotential for plating/stripping and stable cycling of batteries.

The electrochemical stability was also investigated *via* linear scan voltammetry (LSV) measurement. As shown in Fig. 3f, SPE begins oxidative decomposition at ~4.9 V *vs.* Li$^+$/Li, while the electrochemical stable windows of Zeo/PEO and 3D Zeo/PEO are extended to 5.1 and 5.7 V, respectively. At 60 °C, the electrochemical stability of all SSEs undergoes a slight reduction as shown in Fig. S15, due to the enhanced molecular motion and reactivity at high temperature. Nevertheless, 3D Zeo/PEO CSE maintains electrochemical stability with an oxidative decomposition voltage of 5.1 V *vs.* Li$^+$/Li, superior to Zeo/PEO (4.8 V) and SPE (4.4 V). The high oxidation resistance of the zeolite and the reduced reactivity of polymer chains through the interaction with 3D Zeo are both responsible for the high electrochemical stability of 3D Zeo/PEO CSE, which is beneficial for matching high-voltage cathodes to achieve high energy density of batteries.

To further evaluate the electrochemical stability against lithium dendrite growth, symmetric Li|SSEs|Li cells were subjected to galvanostatic cycling under stepwise increased current densities. As shown in Fig. 3g, the critical current density (CCD) values for the SPE, Zeo/PEO, and 3D Zeo/PEO systems are determined to be 0.18, 0.30, and 0.42 mA cm^{-2}, respectively. The relatively low CCD of the Li|SPE|Li cell indicates the insufficient mechanical strength and poor interfacial stability of the pristine SPE with lithium metal electrodes. The improved CCDs for zeolite-based systems reveal the effective dendrite suppression of zeolite-based CSEs, which not only benefits from the improved mechanical strength due to the rigid zeolites but also from the uniform Li$^+$ distribution regulated by the porous zeolites, especially for the 3D Zeo/PEO system. These results demonstrate that 3D Zeo/PEO, with high ionic conductivity and electrochemical stability, is expected to enable excellent cycling and rate performance of solid-state batteries.

The reversibility of SSEs and their compatibility towards Li metal anodes were investigated by testing the galvanostatic charge and discharge performance of Li|SSEs|Li symmetric cells. At a current density of 0.05 mA cm^{-2} with a fixed areal capacity of 0.05 mAh cm^{-2} (Fig. 4a), the Li|SPE|Li cell short-circuits after 155 h of repeated plating/stripping cycles, indicating poor interfacial compatibility and limited mechanical strength of the pristine SPE. In comparison, the Li|Zeo/PEO|Li
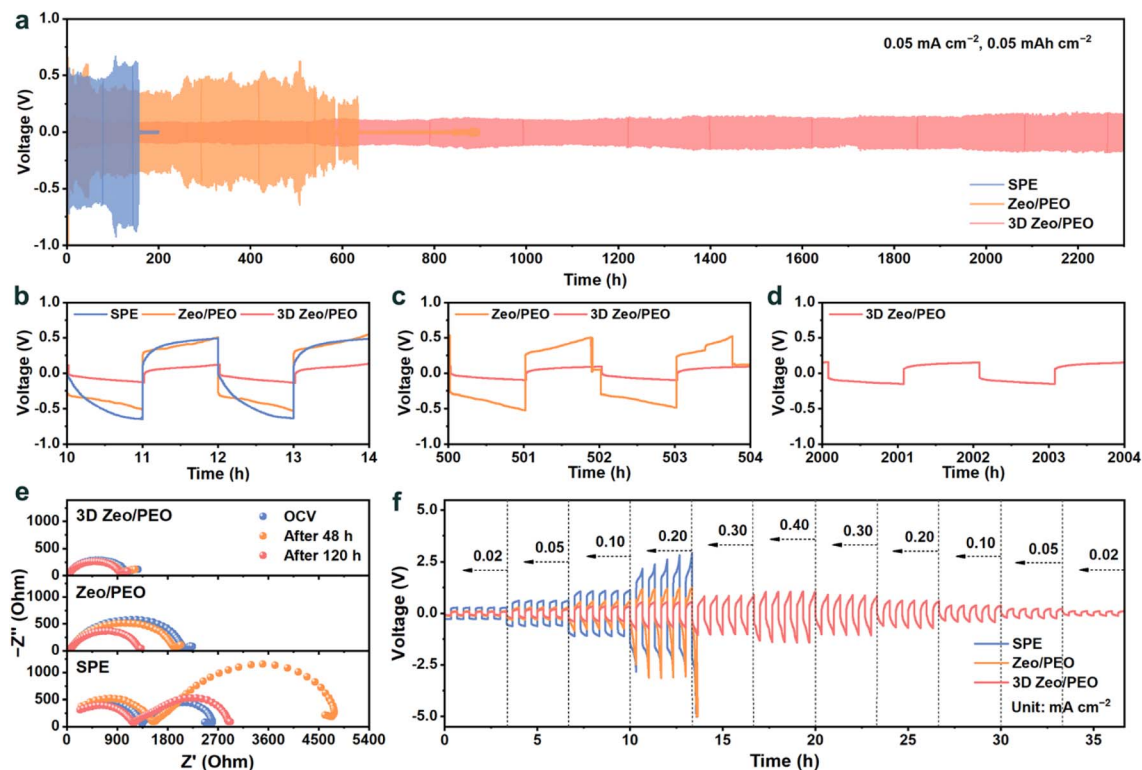
Fig. 4 (a) Galvanostatic Li plating/stripping profiles of SPE, Zeo/PEO, and 3D Zeo/PEO symmetric cells at 0.05 mA cm^{-2} and 0.05 mAh cm^{-2}. (b–d) Enlarged voltage profiles of symmetric cells at different cycling times of (b) 10–14 h, (c) 500–504 h, and (d) 2000–2004 h. (e) Nyquist plots of SPE, Zeo/PEO, and 3D Zeo/PEO symmetric cells at the OCV stage, and after 48 and 120 h of cycling. (f) Galvanostatic charge and discharge profiles of symmetric cells with SPE, Zeo/PEO, and 3D Zeo/PEO at different current densities.

cell shows a prolonged cycling lifespan of about 580 h, and completely fails after 635 h. The 3D Zeo/PEO symmetric cell demonstrates superior cycling stability for over 2300 h, suggesting that 3D Zeo can effectively suppress the lithium dendrites to achieve high reversibility of batteries. The selected voltage profiles of the symmetric cells at different cycling times (Fig. 4b–d) show that the battery using zeolite-based CSEs exhibits a much more stable plating and stripping voltage in comparison with the battery with SPE. As shown in Fig. 4b, SPE, Zeo/PEO, and 3D Zeo/PEO symmetric cells exhibit overpotentials of 0.52, 0.39, and 0.09 V, respectively. This result reflects that the Li|3D Zeo/PEO|Li cell exhibits enhanced Li plating and stripping kinetics compared to the other two systems, owing to the facile bulk and interfacial ionic conduction provided by the 3D Zeo with continuous ion migration pathways and high compatibility with lithium metal. Although the Zeo/PEO symmetric cell remains operational after 500 h, it shows significant voltage fluctuation (Fig. 4c). By contrast, the 3D Zeo/PEO symmetric cell exhibits stable plating/stripping voltage with a small overpotential of 0.13 V even after 2000 h of cycling (Fig. 4d), confirming the excellent long-term interfacial stability of 3D Zeo/PEO CSE.

EIS was conducted to investigate the interfacial resistance evolution upon cycling. As depicted in Fig. 4e, the interfacial impedance of the SPE symmetric cell increases significantly after 48 h due to the undesirable electrochemical stability of SPE and its poor compatibility with the Li metal anode. Then,

the impedance of the SPE symmetric cell decreases after 120 h, but it still higher than that at the open-circuit voltage (OCV) stage, implying the deteriorated charge transfer kinetics at the SPE–Li metal interface. In comparison, the interfacial impedances of zeolite-based CSEs exhibit a decreasing tendency upon cycling, resulting from the improved stability of CESs against the Li metal anode. As the impedance of the 3D Zeo/PEO symmetric cell remains relatively unchanged upon cycling, it suggests that 3D Zeo can effectively suppress interface degradation and preserve continuous ionic conduction pathways.

The galvanostatic charge and discharge profiles of symmetric cells were recorded at various current densities (Fig. 4f) to estimate the rate performance of SSEs. The polarization of the Li|3D Zeo/PEO|Li cell is much lower than that of the Li|SPE|Li cell, indicating a superior plating/stripping kinetics of 3D Zeo/PEO compared to SPE. When the current density increases to 0.30 mA cm^{-2}, the overpotentials of Li|-SPE|Li and Li|Zeo/PEO|Li cells increase to over 5 V, while the overpotential of the Li|3D Zeo/PEO|Li cell is only 0.84 V at 0.40 mA cm^{-2}. The cycling performance of the Li|3D Zeo/PEO|Li cell was also evaluated at 0.10 mA cm^{-2} and 0.10 mAh cm^{-2} (Fig. S16). The plating/stripping overpotential is about 0.25 V after 1000 h, implying superior cycling stability at higher rates. These results manifest that the incorporation of 3D Zeo effectively improves the interfacial compatibility with the Li metal anode, and significantly enhances the Li$^+$ migration in the bulk CSE and at the CSE–electrode interface.

To intuitively elucidate the regulation of 3D Zeo/PEO on Li deposition behavior, the morphology of the Li anode surface after cycling was analyzed *via* SEM. As shown in Fig. 5a, the surface of the Li metal anode from the cycled SPE symmetric cell displays uneven morphology with obvious dendrite formation. In contrast, the Li metal anode of the cycled Zeo/PEO symmetric cell exhibits a relatively flat surface but retains distinct protrusions (Fig. 5b), demonstrating the limited regulatory capability of Zeo/PEO in Li$^+$ deposition. Remarkably, the Li anode from the cycled 3D Zeo/PEO symmetric cell maintains a dense and crack-free surface morphology (Fig. 5c), suggesting uniform Li$^+$ deposition and the formation of a robust SEI layer on the Li metal anode. The capability of zeolite-based CSEs to regulate Li$^+$ deposition behavior presumably stems from the microporous structure of

zeolites, and the migration of Li$^+$ can also be modulated by the interaction between zeolites and the polymer phase, which also explains why 3D Zeo exhibits superior performance in regulating Li$^+$ flux and thus suppressing dendrite growth.

To gain further insight into the chemical composition and valence state of the SEI, X-ray photoelectron spectroscopy (XPS) was conducted on the cycled Li anodes (Fig. 5d–g). In the C 1s spectra (Fig. 5d), all samples reveal typical organic component features in the SEI layers, including peaks for C–C/C–H (284.8 eV), C–O (286.3 eV), and C=O (288.7 eV) originating from the decomposition of PEO.[39,40] In the C 1s spectrum of the Li metal anode cycled with SPE, an intense Li$_2$CO$_3$ signal is observed, reflecting excessive parasitic reactions and poor interfacial stability between the Li metal anode and SPE. Also, the presence
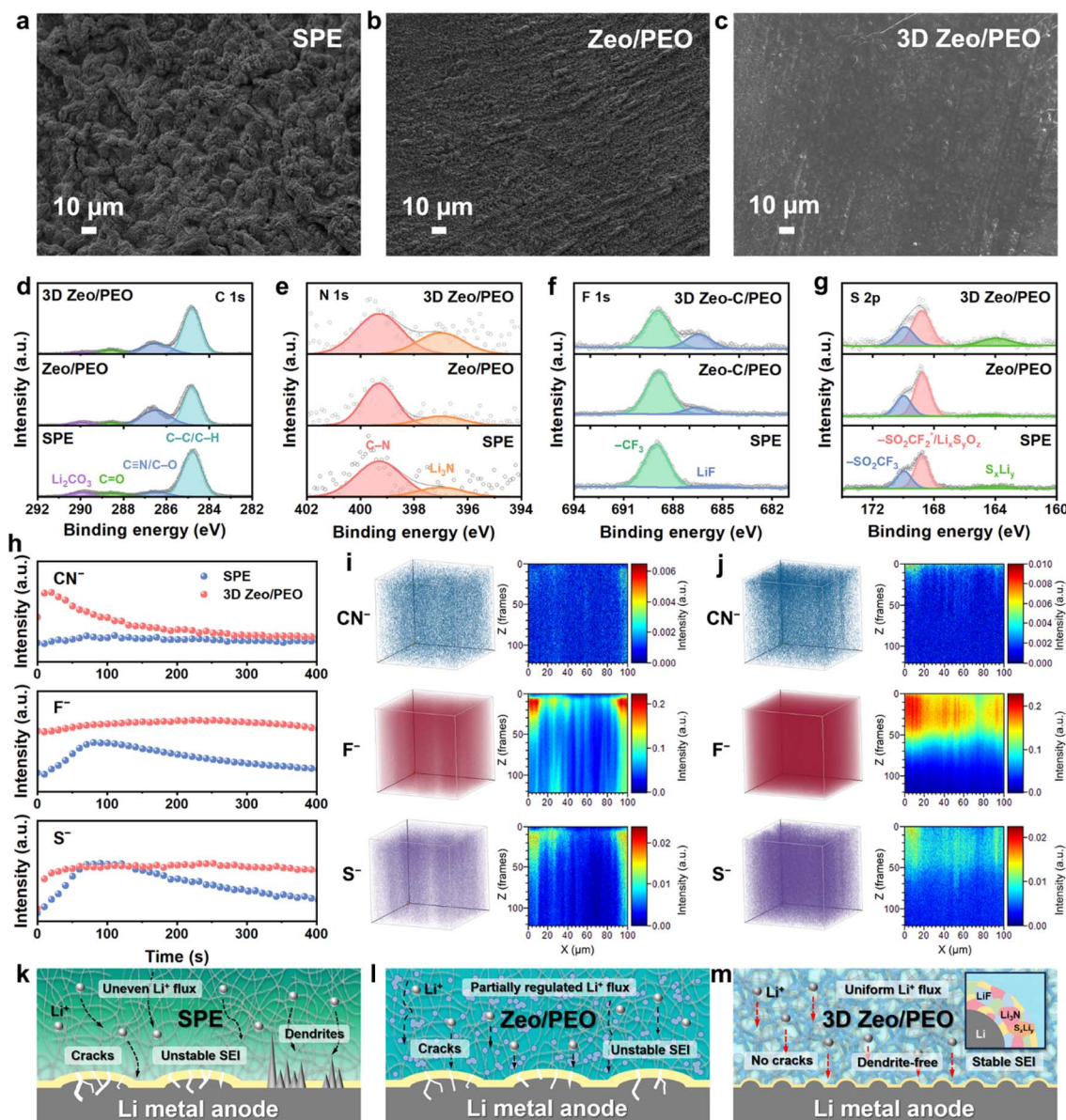

Fig. 5 SEM images of cycled Li anodes in symmetric cells with (a) SPE, (b) Zeo/PEO, and (c) 3D Zeo/PEO. High-resolution (d) C 1s, (e) N 1s, (f) F 1s, and (g) S 2p XPS spectra of cycled Li anodes in SPE, Zeo/PEO, and 3D Zeo/PEO symmetric cells. (h) TOF-SIMS depth profiles for CN$^-$, F$^-$, and S$^-$. 3D distribution mapping and corresponding cross-sectional 2D mappings of the sputtered volume on the SEI using (i) SPE and (j) 3D Zeo/PEO. Schematic illustration of Li deposition behaviours in the cell with (k) SPE, (l) Zeo/PEO, and (m) 3D Zeo/PEO.

of Li_2CO_3 with low ionic conductivity in SEI layers probably leads to short life span and large polarization for the plating/stripping cycles. The carbonate content is diminished in the spectrum of the Li anode cycled with 3D Zeo/PEO CSE, implying the formation of a more stable and uniform SEI layer. The N 1s spectra (Fig. 5e) reveal two peaks at about 396.9 and 399.2 eV, corresponding to Li_3N and C–N from the decomposition of LiTFSI, respectively.[37] The intensity of the Li_3N signal is significantly higher for the spectrum of the Li anode cycled with 3D Zeo/PEO than those of Li anodes cycled with SPE and Zeo/PEO. Taking advantage of the high ionic conductivity and electronic insulation of the Li_3N component, the Li_3N-rich SEI can facilitate Li^+ transport and reduce interfacial resistance, which achieves superior cycling performance of the 3D Zeo/PEO symmetric cell with a low plating/stripping overpotential. In the F 1s spectra, a peak corresponding to LiF ($\sim$686.5 eV) can be observed in addition to the peak at 688.9 eV owing to $-CF_3$ (Fig. 5f),[41,42] and the intensity of this LiF peak markedly increases in the spectrum of Li cycled with 3D Zeo/PEO. The formation of the LiF-rich SEI layer is widely recognized for its high mechanical modulus, low electronic conductivity, and chemical inertness, which is favourable for stabilizing the Li interface. The S 2p spectra (Fig. 5g) reveal a distinct peak at $\sim$163.7 eV in the spectrum of the 3D Zeo/PEO system, which is attributed to Li_2S/Li_xS_y species.[39,43] These inorganic sulfide components suggest a well-regulated decomposition of the LiTFSI salt by 3D Zeo, and are favourable for constructing a mechanically robust and electronically insulating SEI layer to suppress the growth of lithium dendrites.

Time-of-flight secondary ion mass spectrometry (TOF-SIMS) was performed to further investigate the distribution of each component in the SEI on the surface of cycled Li anodes. As shown in Fig. 5h, the contents of CN^-, F^- and S^- in the SEI of 3D Zeo/PEO are consistently higher than those in the SEI of SPE. This indicates the formation of an inorganic-rich SEI consisting of Li_3N, LiF and Li_xS_y, which confirms the XPS results. The 3D distribution mapping and corresponding 2D mappings reveal the spatial distribution of SEI components (Fig. 5i, j and S17). In contrast to SPE, the distribution of these inorganic components in the SEI of 3D Zeo/PEO is more homogeneous with higher content, demonstrating the dense and uniform SEI on the Li anode using 3D Zeo/PEO CSE. Such a uniform inorganic-rich SEI is beneficial to inhibiting continuous interfacial side reactions between the solid electrolyte and the Li anode. Moreover, the signal of CH^- (derived from the decomposition of organic components) in the SEI of 3D Zeo/PEO exhibits a spatial distribution with higher content in the outer layer and lower content in the inner layer (Fig. S18). In contrast, the high content of CH^- in the SEI of SPE indicates the formation of an organic-dominant SEI with inferior mechanical strength, electrochemical stability and Li^+ transport capability.

These findings are visually summarized in the schematic illustrations shown in Fig. 5k–m. In conventional SPE systems (Fig. 5k), the poor compatibility of SPE with the Li metal anode leads to the formation of an unstable SEI layer with high interfacial resistance. Also, the inferior mechanical strength of SPE and the uneven Li^+ flux in the SPE with low ionic conductivity

result in the inevitable lithium dendrite growth. Therefore, the SPE symmetric cell presents a high plating/stripping overpotential, and even short-circuits after less than 160 h. In virtue of the incorporation of zeolite particles with the polymer phase, the Zeo/PEO CSE (Fig. 5l) displays a moderate effect on improving the ionic conduction and alleviating the dendrite growth. Unfortunately, limited by the composite method of physical blending, Zeo/PEO CSE fails to provide continuous ion-conducting pathways and sufficient coordinating capability to improve the compatibility with Li metal, leading to uneven deposition and partial SEI collapse on the Li anode. In sharp contrast, the introduction of 3D Zeo effectively boosts ion transport *via* various pathways, homogenizes Li^+ flux to achieve uniform deposition, and directs SEI formation to improve the interfacial compatibility with Li metal (Fig. 5m). Taking advantage of the rational design of the 3D architecture and the coordinating regulation effect of 3D Zeo, the 3D Zeo/PEO CSE is favourable to achieve dendrite-free and high-performance solid-state LMBs.

To further evaluate the practical electrochemical performance of the SSEs, full cells were assembled using LFP as the cathode and lithium metal as the anode. As shown in Fig. 6a and b, the LFP|3D Zeo/PEO|Li full cell delivers an initial specific capacity of 169 mAh g^{-1} at 0.1C, which is much higher than that of the LFP|SPE|Li full cell (69 mAh g^{-1}) at RT. Also, the charging–discharging voltage hysteresis of the LFP|3D Zeo/PEO|Li full cell (0.4 V) is considerably lower in comparison with that of the LFP|SPE|Li full cell (1.0 V), indicating a fast electrochemical reaction kinetics of the batteries with 3D Zeo/PEO CSE. As the cycles proceed, the charge and discharge plateaus of the full cell with SPE gradually deteriorate, whereas the full cell with 3D Zeo/PEO CSE demonstrates well-defined plateaus with a slight increase in the charging–discharging polarization. After 100 cycles, the specific capacity of the LFP|SPE|Li full cell plummets to below 5 mAh g^{-1}, while the LFP|3D Zeo/PEO|Li full cell delivers a specific capacity of 154 mAh g^{-1}, corresponding to a capacity retention of 91% (Fig. 6c).

Additionally, the 3D Zeo/PEO CSE manifests excellent rate performance as shown in Fig. 6d. The 3D Zeo/PEO-based full cell delivers the capacities of 165, 164, 149, 122, and 97 mAh g^{-1} at 0.1C, 0.2C, 0.3C, 0.5C, and 1.0C, respectively. In contrast, the SPE-based full cell fails to sustain any significant specific capacity beyond 0.2C. When the current density is recovered to 0.1C, the 3D Zeo/PEO-based full cell demonstrates a specific capacity of 170 mAh g^{-1}, which is slightly higher than the initial specific capacity. This might be attributed to the activation process of the battery, revealing the high reversibility of the 3D Zeo/PEO CSE. The cycling performance at higher C-rates also confirms the superior electrochemical performance of the 3D Zeo/PEO-based full cell (Fig. S19). In particular, the 3D Zeo/PEO-based full cell achieves a capacity retention of 92% after 500 cycles at 0.5C, which is in sharp contrast with the poor electrochemical performance of the SPE-based full cell (Fig. 6e and S20).

The electrochemical performance of the SSEs was also evaluated at 60 °C, under which conditions the segmental motion of the polymer is more active. As shown in Fig. 6f, the LFP|3D Zeo/PEO|Li full cell exhibits a stable cycling performance at 1.0C
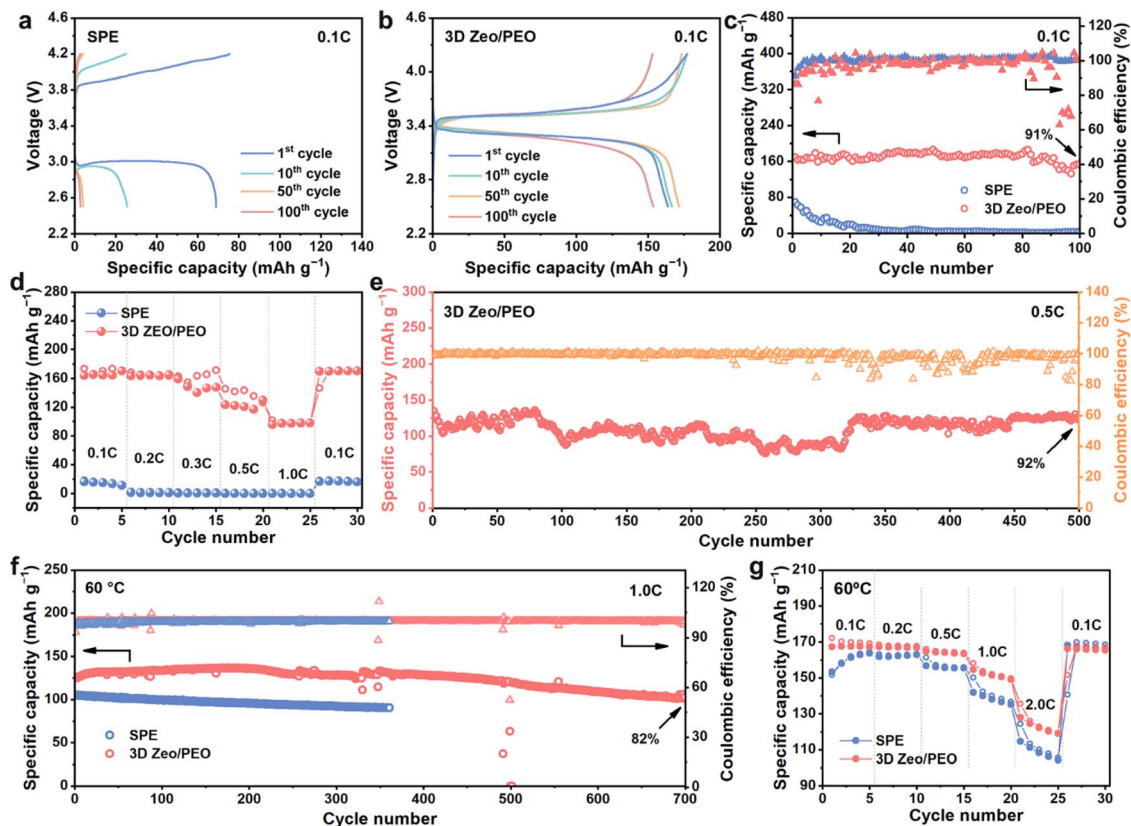
Fig. 6 Galvanostatic charge and discharge profiles of LFP|SSEs|Li full cells with (a) SPE and (b) 3D Zeo/PEO at 0.1C and RT (1C = 170 mA g^{-1}). (c) Cycling performance at 0.1C and (d) rate performance of SPE and 3D Zeo/PEO full cells at RT. (e) Cycling performance of the LFP|3D Zeo/PEO|Li full cell at 0.5C and RT. (f) Cycling performance at 1.0C and (g) rate performance of SPE and 3D Zeo/PEO full cells at 60 °C.

with a capacity retention of 82% after 700 cycles. Although the 3D Zeo/PEO-based cell shows a capacity fading tendency at 60 °C compared with that at RT probably due to the instability and thus interfacial degradation of the active polymer (Fig. S21–23), it retains a higher specific capacity than that of the SPE-based cell. Also, the 3D Zeo/PEO-based cell displays superior rate capability (Fig. 6g and S24) and comparable cycling performance at a higher C-rate of 2.0C (Fig. S25), confirming the superior interfacial compatibility and ionic conductivity of the 3D Zeo/PEO CSE compared to the conventional SPE. Moreover, the compatibility of SSEs with a high-voltage LiNi$_{0.8}$Co$_{0.1}$Mn$_{0.1}$O$_2$ (NCM) cathode was evaluated as shown in Fig. S26. The NCM|SPE|Li full cell exhibits inferior cycling capability due to the poor electrochemical stability of SPE, as evidenced by its coulombic efficiency of only 96.8% after 100 cycles. In sharp contrast, the NCM|3D Zeo/PEO|Li full cell demonstrates a specific capacity of 168 mAh g^{-1} at 1.0C after 100 cycles, corresponding to a capacity retention of 87% with a stable coulombic efficiency of over 99%. These results further confirm the outstanding stability and compatibility of 3D Zeo/PEO with high-voltage cathodes compared to SPE.

Conclusions

In summary, we report a composite solid-state electrolyte, 3D Zeo/PEO, constructed by integrating a 3D zeolite network into a LiTFSI–PEO matrix, achieving concurrent improvements in ionic conductivity, electrochemical stability, and interfacial compatibility. The 3D zeolite network provides continuous Li$^+$ conduction pathways and promotes salt dissociation and polymer chain disorder *via* Lewis acid–base interactions. As a result, the 3D Zeo/PEO CSE enables dendrite-free lithium cycling over 2300 h and superior performance with high capacity retention at both ambient (92% at 0.5C after 500 cycles) and elevated temperatures (82% at 1.0C after 700 cycles), far exceeding those of the batteries with SPE and Zeo/PEO SSEs. The superior performance is attributed to the excellent capability of 3D Zeo/PEO CSE to regulate the distribution of Li$^+$ flux and induce the formation of a stable SEI with superior ionic transport kinetics, revealing the rational design of a 3D structured zeolite network with high stability and ionic conduction. This work proposes a promising design strategy of CSEs by employing a 3D zeolite network, which provides a new insight into simultaneously achieving the high ionic conductivity, stability, and interfacial compatibility of CSEs for high-performance solid-state lithium metal batteries.

Author contributions

Z. Luo designed and conducted the experiments, performed the data analysis, and drafted the manuscript; Y. Cui conducted the experiments and assisted with data discussion and analysis; Z.

Zhang participated in the data discussion and analysis; M. Li was responsible for the supervision, data curation, validation, visualization, manuscript revision, and funding acquisition; J. Yu conceived and supervised the research, and contributed to methodology development, manuscript revision, and funding acquisition.

Conflicts of interest

There are no conflicts to declare.

Data availability

The data supporting this article have been included as part of the supplementary information (SI). Supplementary information: materials and experimental details, characterisation data, and electrochemical performance data (Fig. S1–S26 and Table S1). See DOI: https://doi.org/10.1039/d5sc05786h.

Acknowledgements

References

1 G. G. Njema, R. B. O. Ouma and J. K. Kibet, A review on the recent advances in battery development and energy storage technologies, *J. Renewable Energy*, 2024, **2024**, 2329261.

2 B. Liu, J.-G. Zhang and W. Xu, Advancing lithium metal batteries, *Joule*, 2018, **2**, 833–845.

3 Z. Zhang and W.-Q. Han, From liquid to solid-state lithium metal batteries: fundamental issues and recent developments, *Nano-Micro Lett.*, 2024, **16**, 24.

4 J. Yu, Y. Wang, L. Shen, J. Liu, Z. Wang, S. Xu, H. M. Law and F. Ciucci, Fast-charging solid-state Li batteries: materials, strategies, and prospects, *Adv. Mater.*, 2025, **37**, 2417796.

5 H. Wan, Z. Wang, S. Liu, B. Zhang, X. He, W. Zhang and C. Wang, Critical interphase overpotential as a lithium dendrite-suppression criterion for all-solid-state lithium battery design, *Nat. Energy*, 2023, **8**, 473–481.

6 H. Adenusi, G. A. Chass, S. Passerini, K. V. Tian and G. Chen, Lithium batteries and the solid electrolyte interphase (SEI)—progress and outlook, *Adv. Energy Mater.*, 2023, **13**, 2203307.

7 Y. Jie, X. Ren, R. Cao, W. Cai and S. Jiao, Advanced liquid electrolytes for rechargeable Li metal batteries, *Adv. Funct. Mater.*, 2020, **30**, 1910777.

8 N. Li, X. Han, X. Cui, C. Xu, C. Mao, X. Dai and W. Xue, Recent progress in liquid electrolytes for high-energy lithium–metal batteries: from molecular engineering to applications, *Adv. Funct. Mater.*, 2025, **35**, 2409431.

9 X. Fan and C. Wang, High-voltage liquid electrolytes for Li batteries: progress and perspectives, *Chem. Soc. Rev.*, 2021, **50**, 10486–10566.

10 S. Lei, Z. Zeng, S. Cheng and J. Xie, Fast-charging of lithium-ion batteries: a review of electrolyte design aspects, *Battery Energy*, 2023, **2**, 20230018.

11 S. Raza, T. Bashir, A. Hayat, H. S. M. Abd-Rabboh, L. Shen, Y. Orooji and H. Lin, Recent progress and fundamentals of solid-state electrolytes for all solid-state rechargeable batteries: mechanisms, challenges, and applications, *J. Energy Storage*, 2024, **92**, 112110.

12 Z. Xue, D. He and X. Xie, Poly(ethylene oxide)-based electrolytes for lithium-ion batteries, *J. Mater. Chem. A*, 2015, **3**, 19218–19253.

13 X. Su, X.-P. Xu, Z.-Q. Ji, J. Wu, F. Ma and L.-Z. Fan, Polyethylene oxide-based composite solid electrolytes for lithium batteries: current progress, low-temperature and high-voltage limitations, and prospects, *Electrochem. Energy Rev.*, 2024, **7**, 2.

14 Y. An, X. Han, Y. Liu, A. Azhar, J. Na, A. K. Nanjundan, S. Wang, J. Yu and Y. Yamauchi, Progress in solid polymer electrolytes for lithium-ion batteries and beyond, *Small*, 2022, **18**, 2103617.

15 C.-Z. Zhao, X.-Q. Zhang, X.-B. Cheng, R. Zhang, R. Xu, P.-Y. Chen, H.-J. Peng, J.-Q. Huang and Q. Zhang, An anion-immobilized composite electrolyte for dendrite-free lithium metal anodes, *Proc. Natl. Acad. Sci. U. S. A.*, 2017, **114**, 11069–11074.

16 G. Wang, H. Liu, Y. Liang, C. Wang and L.-Z. Fan, Composite polymer electrolyte with three-dimensional ion transport channels constructed by NaCl template for solid-state lithium metal batteries, *Energy Storage Mater.*, 2022, **45**, 1212–1219.

17 Z. Hong, P. Li, Q. Zou, L. Gu, J. Wang, L. Deng, C. Wang, Y. Zhang, M. Li, J. Chen, R. Si and C. Yang, Metal organic framework (MOF-808) incorporated composite polymer electrolyte for stable all-solid-state lithium batteries, *ACS Appl. Energy Mater.*, 2024, **7**, 11967–11976.

18 W. Hu, P.-H. Chien, N. Wu and S. Zhong, High Li^+ conducting porous garnet enables fast Li^+ conduction in polymer/garnet composite electrolyte, *ACS Appl. Energy Mater.*, 2024, **7**, 8077–8084.

19 F. Gui, X. Zhou, K. Huang, X. Li, Z. Yan, Z. Luo, L. Yang, J. Huang, G. Wang, G. Xu and X. Ou, Tailoring the ionic conductivity of composite electrolyte by La-doping regulated $Li_4Ti_5O_{12}$ for solid state lithium metal batteries, *Acta Mater.*, 2025, **286**, 120720.

20 S. Wen, Z. Sun, X. Wu, S. Zhou, Q. Yin, H. Chen, J. Pan, Z. Zhang, Z. Zhuang, J. Wan, W. Zhou, D.-L. Peng and Q. Zhang, Regulating interfacial chemistry to boost ionic transport and interface stability of composite solid-state electrolytes for high-performance solid-state lithium metal batteries, *Adv. Funct. Mater.*, 2025, **35**, 2422147.

21 W. Fan, J. Gou, Y. Huang, K. She, M. Yu and Z. Zhang, "Peapod-like" fiber network: a universal strategy for composite solid electrolytes to inhibit lithium dendrite growth in solid-state lithium metal batteries, *Nano Lett.*, 2024, **24**, 9050–9057.

22 Y. Zheng, Y. Yao, J. Ou, M. Li, D. Luo, H. Dou, Z. Li, K. Amine, A. Yu and Z. Chen, A review of composite solid-state

electrolytes for lithium batteries: fundamentals, key materials and advanced structures, *Chem. Soc. Rev.*, 2020, **49**, 8790–8839.

23 J. Zheng and Y.-Y. Hu, New insights into the compositional dependence of Li-ion transport in polymer–ceramic composite electrolytes, *ACS Appl. Mater. Interfaces*, 2018, **10**, 4113–4120.

24 K. Liu, M. Wu, L. Wei, Y. Lin and T. Zhao, A composite solid electrolyte with a framework of vertically aligned perovskite for all-solid-state Li-metal batteries, *J. Membr. Sci.*, 2020, **610**, 118265.

25 Y. Fu, Z. Gu, Q. Gan and Y.-W. Mai, A review on the ionic conductivity and mechanical properties of composite polymer electrolytes (CPEs) for lithium batteries: insights from the perspective of polymer/filler composites, *Mater. Sci. Eng. R*, 2024, **160**, 100815.

26 X. Chi, M. Li, J. Di, P. Bai, L. Song, X. Wang, F. Li, S. Liang, J. Xu and J. Yu, A highly stable and flexible zeolite electrolyte solid-state Li–air battery, *Nature*, 2021, **592**, 551–557.

27 X. Chi, M. Li, X. Chen, J. Xu, X. Yin, S. Li, Z. Jin, Z. Luo, X. Wang, D. Kong, M. Han, J.-J. Xu, Z. Liu, D. Mei, J. Wang, G. Henkelman and J. Yu, Enabling high-performance all-solid-state batteries via guest wrench in zeolite strategy, *J. Am. Chem. Soc.*, 2023, **145**, 24116–24125.

28 W. Yang, Y. Liu, X. Sun, Z. He, P. He and H. Zhou, Solvation-tailored PVDF-based solid-state electrolyte for high-voltage lithium metal batteries, *Angew. Chem., Int. Ed.*, 2024, **63**, e202401428.

29 Z. Ding, Q. Tang, Q. Zhang, P. Yao, X. Liu and J. Wu, A flexible solid polymer electrolyte enabled with lithiated zeolite for high performance lithium battery, *Nano Res.*, 2023, **16**, 9443–9452.

30 W. Li, S. Zhang, B. Wang, S. Gu, D. Xu, J. Wang, C. Chen and Z. Wen, Nanoporous adsorption effect on alteration of the Li^+ diffusion pathway by a highly ordered porous electrolyte additive for high-rate all-solid-state lithium metal batteries, *ACS Appl. Mater. Interfaces*, 2018, **10**, 23874–23882.

31 H. Jamal, F. Khan, S. Hyun, S. W. Min and J. H. Kim, Enhancement of the ionic conductivity of a composite polymer electrolyte *via* surface functionalization of SSZ-13 zeolite for all-solid-state Li-metal batteries, *J. Mater. Chem. A*, 2021, **9**, 4126–4137.

32 H. Jamal, F. Khan, H.-R. Si and J. H. Kim, Enhanced compatibility of a polymer-based electrolyte with Li-metal for stable and dendrite-free all-solid-state Li-metal batteries, *J. Mater. Chem. A*, 2021, **9**, 27304–27319.

33 J. M. K. W. Kumari, G. K. R. Senadeera, A. M. J. S. Weerasinghe, C. A. Thotawatthage and M. A. K. L. Dissanayake, Effect of polyaniline (PANI) on

34 Z. Xu, T. Yang, X. Chu, H. Su, Z. Wang, N. Chen, B. Gu, H. Zhang, W. Deng, H. Zhang and W. Yang, Strong Lewis acid–base and weak hydrogen bond synergistically enhancing ionic conductivity of poly(ethylene oxide)@SiO_2 electrolytes for a high rate capability Li-metal battery, *ACS Appl. Mater. Interfaces*, 2020, **12**, 10341–10349.

35 G. Wang, X. Zhu, A. Rashid, Z. Hu, P. Sun, Q. Zhang and L. Zhang, Organic polymeric filler-amorphized poly(ethylene oxide) electrolyte enables all-solid-state lithium–metal batteries operating at 35 °C, *J. Mater. Chem. A*, 2020, **8**, 13351–13363.

36 Y. Zou, Z. Ao, Z. Zhang, N. Chen, H. Zou, Y. Lv and Y. Huang, Metal-organic framework modified PEO-based solid electrolyte for high-performance all-solid-state lithium metal batteries, *Chem. Eng. Sci.*, 2023, **275**, 118705.

37 S. Li, F. Pei, Y. Ding, X. Guo, X. Zhang, H. Tao, Z. He, H. Hu and L. Zhang, Metal-organic framework-derived elastic solid polymer electrolytes enabled by covalent crosslinking for high-performance lithium metal batteries, *Adv. Funct. Mater.*, 2025, **35**, 2415495.

38 N. Chen, Y. Dai, Y. Xing, L. Wang, C. Guo, R. Chen, S. Guo and F. Wu, Biomimetic ant-nest ionogel electrolyte boosts the performance of dendrite-free lithium batteries, *Energy Environ. Sci.*, 2017, **10**, 1660–1667.

39 Y. Chai, D. Ning, D. Zhou, J. Gao, J. Ni, G. Zhang, R. Gao, W. Wu, J. Wang and Y. Li, Construction of flexible asymmetric composite polymer electrolytes for high-voltage lithium metal batteries with superior performance, *Nano Energy*, 2024, **130**, 110160.

40 Z. Geng, Y. Huang, G. Sun, R. Chen, W. Cao, J. Zheng and H. Li, In-situ polymerized solid-state electrolytes with stable cycling for Li/$LiCoO_2$ batteries, *Nano Energy*, 2022, **91**, 106679.

41 F. J. Simon, M. Hanauer, F. H. Richter and J. Janek, Interphase formation of PEO_{20}:$LiTFSI$–Li_6PS_5Cl composite electrolytes with lithium metal, *ACS Appl. Mater. Interfaces*, 2020, **12**, 11713–11723.

42 I. Jeong, S. Kim, Y. Kim, C. Kim, J. Kang, J. H. Ha, Y. Cho, S. J. Kang, J. Ryu, J. W. Han and S. Park, Toward long-life high-voltage aqueous Li-ion batteries: from solvation chemistry to solid-electrolyte-interphase layer optimization against electron tunneling effect, *Adv. Mater.*, 2025, **37**, 2412652.

43 R. Fang, H. Xu, B. Xu, X. Li, Y. Li and J. B. Goodenough, Reaction mechanism optimization of solid-state Li–S batteries with a PEO-based electrolyte, *Adv. Funct. Mater.*, 2021, **31**, 2001812.